

Reducing Memorisation in Generative Models via Riemannian Bayesian Inference

Johanna Marie Gegenfurtner ^{*1} Albert Kjøller Jacobsen ^{*1}
 Naima Elosegui Borras ¹ Alejandro Valverde Mahou ¹
 Georgios Arvanitidis ¹

Abstract

Modern generative models can produce realistic samples, however, balancing memorisation and generalisation remains an open problem. We approach this challenge from a Bayesian perspective by focusing on the parameter space of flow matching and diffusion models and constructing a predictive posterior that better captures the variability of the data distribution. In particular, we capture the geometry of the loss using a Riemannian metric and leverage a flexible approximate posterior that adapts to the local structure of the loss landscape. This approach allows us to sample generative models that resemble the original model, but exhibit reduced memorisation. Empirically, we demonstrate that the proposed approach reduces memorisation while preserving generalisation. Further, we provide a theoretical analysis of our method, which explains our findings. Overall, our work illustrates how considering the geometry of the loss enables effective use of the parameter space, even for complex high-dimensional generative models.

1. Introduction

The success of modern generative models has raised questions about their capacity to merely memorise data or generate beyond it. While it is essential that a generative model captures the data distribution, it is critical in several applications to avoid overfitting to specific training examples. For predictive models, overfitting to the training data can boost performance as seen from the double descent phenomenon, however, there is no such thing as benign overfitting in the context of generative modelling, as perfectly replicating

^{*}Equal contribution ¹Department of Applied Mathematics and Computer Science, Technical University of Denmark. Correspondence to: Johanna Marie Gegenfurtner <johge@dtu.dk>, Albert Kjøller Jacobsen <akjja@dtu.dk>.

Preprint. February 3, 2026.

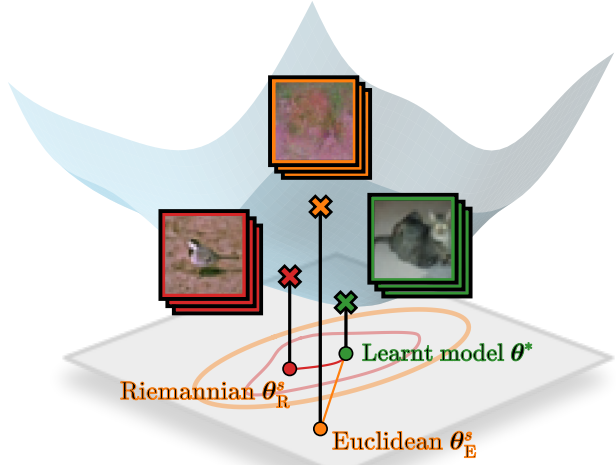


Figure 1. We propose reducing memorisation of a trained generative model by perturbing the learnt model parameters θ^* (●) by sampling from an approximate posterior distribution $\theta \sim q(\theta)$, thus constructing new models. While samples from a Euclidean approximate posterior (○) reduce memorisation, accounting for the geometry (●) reduces memorisation without breaking the fit.

training data points raises concerns about privacy. Our work focuses on diffusion models, for which the problem of memorisation has been extensively discussed in recent work (Liu et al., 2024). In this paper, we raise the question:

Can we reduce memorisation in modern generative models through uncertainty on their parameters?

To mitigate memorisation in modern generative models, we adopt a Bayesian treatment of the model parameters, using the Laplace approximation (LA) for defining a conceptually simple approximate posterior distribution. The Laplace approximation is defined as a Gaussian centred at the maximum a posteriori (MAP) estimate, however, it is often an overly crude approximation of the true posterior. To address this issue, we make use of the Riemannian Laplace approximation (Bergamin et al., 2023) that leverages the geometric structure of the true posterior. This allows us to perturb the parameters of the learnt model and construct an ensemble of

generators, where each member reduces memorisation compared to the original model. As Bertrand et al. (2025) have shown, generalisation happens exactly when the models fails to overfit to the training objective – we achieve generalisation by breaking the overfitting behaviour. Through experiments on flow matching and diffusion models, we demonstrate that introducing uncertainty on the model parameters while respecting the true posterior geometry is an effective way to reduce memorisation without forgetting how to generalise.

Specifically, our contributions are:

1. We define a geometry-informed approximate posterior distribution over model parameters of diffusion-like generative models (Subsection 2.2.1).
2. We extend a method for estimating generative uncertainty (Jazbec et al., 2025). For deterministic generators, we define the exact likelihood of a generated sample (Subsection 3.1).
3. We provide mathematically grounded explanations on how our approach mitigates memorisation, and why a Riemannian perspective outperforms the standard Laplace approximation (Section 4).
4. We provide empirical evidence that respecting the geometric structure can help generative models *generalise rather than memorise*, as our posterior predictive is based on parameter samples from high-density regions of the true posterior (Section 5).

2. Background

2.1. Generative Modelling

Assume we have N data samples $\mathcal{D}_x = \{\mathbf{x}_*^i\}_{i=1}^N \in \mathcal{X} \subseteq \mathbb{R}^D$ from an unknown distribution p_* . When training a generative model, the goal is to find a generator function g_θ that maps samples from a known base distribution $\mathbf{x}_0 \sim p_0$ to new samples $\hat{\mathbf{x}}$ that approximately belong to p_* . Hence, the generative process can be summarised as:

$$\hat{\mathbf{x}} = g_\theta(\mathbf{x}_0), \quad \mathbf{x}_0 \sim p_0. \quad (1)$$

2.1.1. FLOW MATCHING

In flow matching, the generator’s output is the endpoint of the solution of an initial value problem (IVP) of the form

$$\mathbf{x}(0) = \mathbf{x}_0, \quad \dot{\mathbf{x}}(t) = u_\theta(\mathbf{x}_t, t), \quad (2)$$

where $u_\theta : \mathbb{R}^D \times [0, 1] \rightarrow \mathbb{R}^D$ is a velocity field, represented by a neural network with parameters θ . We will denote a generated sample as $\hat{\mathbf{x}} = \mathbf{x}(1)$. Usually, the base distribution is the unit Gaussian distribution $p_0 = \mathcal{N}(\mathbf{0}, \mathbb{I}_D)$

and the IVP is solved with an Euler scheme. We denote the distribution of generated samples by $p(\hat{\mathbf{x}})$.

To learn the velocity field u_θ , we optimise the loss function:

$$\mathcal{L}_{\text{FM}}(\theta, \mathcal{D}_x) = \mathbb{E}_{\substack{\mathbf{x}_0 \sim p_0 \\ \mathbf{x}_* \sim \mathcal{D}_x \\ t \sim \mathcal{U}[0, 1]}} [\|\mathbf{x}_*(t), t) - (\mathbf{x}_* - \mathbf{x}_0)\|_2^2]. \quad (3)$$

For a Gaussian optimal transport path, a sample from the conditional probability path, $\mathbf{x}_t \sim p_t(\cdot | \mathbf{x}_*)$, is given by

$$\mathbf{x}_t = t\mathbf{x}_* + (1 - t)\mathbf{x}_0. \quad (4)$$

Differentiating with respect to time t gives us the target function as in Equation (3). For further reading, see the lecture notes by Holderrieth and Erives (2025).

2.1.2. DIFFUSION MODELS

Under certain conditions, flow matching and denoising diffusion implicit models (DDIM) (Song et al., 2021a) are equivalent at sampling time (Song et al., 2021b; Gao et al., 2024). A diffusion model defines a forward process that gradually transforms data into noise. This process is then reversed to generate samples. Given the extensive literature on diffusion models (Holderrieth and Erives, 2025; Sohl-Dickstein et al., 2015), we focus on DDIM and its relation to flow matching.

Let $p_t(\mathbf{x})$ denote the marginal distribution of a diffusion process at time $t \in [0, 1]$, where $t = 0$ corresponds to the data distribution and $t = 1$ to a standard Gaussian. DDIM sampling can be formulated as the deterministic ODE

$$\dot{\mathbf{x}}(t) = f(t)\mathbf{x}(t) - \frac{1}{2}g(t)^2\nabla_{\mathbf{x}} \log p_t(\mathbf{x}(t)), \quad (5)$$

where $f, g : [0, 1] \rightarrow \mathbb{R}$ define the forward diffusion process and $\nabla_{\mathbf{x}} \log p_t(\mathbf{x})$ is the score function, which is approximated by a neural network $s_\theta(\mathbf{x}(t), t)$.

Under mild regularity assumptions, Gao et al. (2024) reparameterise Equation (5) as a flow matching model:

$$u_\theta(\mathbf{x}(t), t) \equiv f(t)\mathbf{x}(t) - \frac{1}{2}g(t)^2s_\theta(\mathbf{x}(t), t). \quad (6)$$

From this perspective, DDIM sampling is a particular parameterisation of a deterministic flow. This equivalence implies that samples from a diffusion process can be generated using a flow matching model with the appropriate parameterisation, and vice versa. For this reason, we adopt the flow matching formulation throughout.

2.1.3. MEMORISATION IN GENERATIVE MODELS

In this subsection we will define the nearest neighbour memorisation measure. We say that a point is memorised if it is much closer to one point from the training set than to all others (Yoon et al., 2023; Buchanan et al., 2025).

Definition 2.1. A generated data sample, $\hat{\mathbf{x}}$, is memorised if for a fixed threshold $c \in (0, 1)$,

$$\|\hat{\mathbf{x}} - \mathbf{x}^{(1)}(\hat{\mathbf{x}})\|^2 \leq c \|\hat{\mathbf{x}} - \mathbf{x}^{(2)}(\hat{\mathbf{x}})\|^2, \quad (7)$$

where $\mathbf{x}^{(1)}(\hat{\mathbf{x}})$ and $\mathbf{x}^{(2)}(\hat{\mathbf{x}})$ are the closest and second-closest training samples to $\hat{\mathbf{x}}$, respectively.

The corresponding memorisation ratio (Buchanan et al., 2025) of a generative model g_{θ} is given by

$$\frac{1}{N} \sum_{i=1}^N \mathbb{1} \left[\left\| \hat{\mathbf{x}}^i - \mathbf{x}^{(1)}(\hat{\mathbf{x}}^i) \right\|^2 \leq c \left\| \hat{\mathbf{x}}^i - \mathbf{x}^{(2)}(\hat{\mathbf{x}}^i) \right\|^2 \right], \quad (8)$$

where $\{\hat{\mathbf{x}}^i = g_{\theta}(\mathbf{x}_0^i) \mid \mathbf{x}_0^i \sim p_0\}_{i=1}^N$ is a set of N generated data points. As we will discuss in Subsection 6.3, there are several definitions of memorisation – e.g. by accounting for the average distance to the K nearest training samples, and not only the first and second closest (Chen et al., 2024).

2.2. Bayesian Deep Learning

One way to quantify uncertainty of a neural network is to consider the variation in the outputs of an ensemble of learners. However, instead of training multiple neural networks, a common approach is to treat the model parameters in a *Bayesian* manner by defining a posterior distribution over the model parameters using Bayes’ rule. We can consider the negative log-posterior as a loss function given by

$$\mathcal{L}_{\text{post}}(\theta, \mathcal{D}) = -\log \frac{p(\mathcal{D}|\theta) p(\theta)}{p(\mathcal{D})} \quad (9)$$

$$\propto -\log p(\mathcal{D}|\theta) - \log p(\theta). \quad (10)$$

Although the log-posterior is intractable, the fact that the log-joint is proportional to it allows us to define an approximate posterior distribution over the model parameters that respects the local geometry at the optimum. We can define this distribution *post-hoc* using the Laplace approximation:

$$q(\theta|\mathcal{D}) = \mathcal{N}(\theta \mid \theta^*, \mathbf{H}_{\mathcal{L}_{\text{post}}}^{-1}(\theta^*)), \quad (11)$$

where $\theta^* = \arg \min_{\theta} \mathcal{L}_{\text{post}}(\theta)$ is the *maximum a posteriori* (MAP) estimate and $\mathbf{H}_{\mathcal{L}}(\theta) := \nabla_{\theta}^2 \mathcal{L}_{\text{post}}(\theta, \mathcal{D})$ is the Hessian of the posterior loss, which we evaluate at the MAP. We denote a sample from this Euclidean/classic Laplace approximation by $\theta_{\text{E}}^s = \theta^* + \mathbf{v}$ where $\mathbf{v} \sim \mathcal{N}(\mathbf{0}, \mathbf{H}_{\mathcal{L}}^{-1}(\theta^*))$.

2.2.1. THE RIEMANNIAN LAPLACE APPROXIMATION

Bergamin et al. (2023) introduced a Riemannian take on the Laplace approximation, which outperforms the conventional method by respecting the geometric structure of the true posterior. This approach constrains samples from the approximate posterior to lie within high-density regions of the true posterior, while the standard Laplace approximation

has no such guarantee. We explain a few concepts from the field of Riemannian geometry in Appendix A.

Mathematically, the Riemannian Laplace approximation $q_{\mathcal{M}}(\theta|\mathcal{D}) = (f_{\mathcal{M}})_{\#} q(\mathbf{v}|\mathcal{D})$ is the pushforward of a distribution of vectors $q(\mathbf{v}|\mathcal{D}) = \mathcal{N}(\mathbf{v} \mid \mathbf{0}, \mathbf{H}_{\mathcal{L}}^{-1}(\theta^*))$ through a mapping $f_{\mathcal{M}}$. This mapping depends on the geometry of the *loss manifold*, especially on our choice of metric, which defines a way of measuring distances on the manifold.

We define the (posterior) loss manifold as the graph of the posterior loss function given in Equation (10):

$$\mathcal{M} = \{h(\theta) \mid \theta \in \Theta\} \subseteq \mathbb{R}^{(K+1)}. \quad (12)$$

A natural parametrisation of \mathcal{M} is given by

$$h : \Theta \rightarrow \mathbb{R}^{K+1}, \quad h(\theta) = (\theta_1, \dots, \theta_K, \mathcal{L}_{\text{post}}(\theta)). \quad (13)$$

This parametrisation has also been considered in (Hartmann et al., 2022; Jacobsen and Arvanitidis, 2025; Williams et al., 2025), for instance.

For every $\mathbf{v} \sim q(\mathbf{v}|\mathcal{D})$, there exists a curve $\alpha(t) \subseteq \Theta$ starting at $\alpha(0) = \theta^*$ with initial velocity $\dot{\alpha}(0) = \mathbf{v}$ such that $\gamma(t) = (\alpha(t), \mathcal{L}(\alpha(t)))$ is a geodesic (a locally shortest path on the loss manifold \mathcal{M}), as illustrated in Figure 2.

To sample from the Riemannian Laplace approximation, we compute the curve $\alpha(t)$ by solving the *geodesic equation*:

$$\ddot{\alpha}_k(t) = - \sum_{i,j=1}^n \dot{\alpha}_i(t) \dot{\alpha}_j(t) \cdot \Gamma_{ij}^k(\alpha(t)), \quad (14)$$

where Γ_{ij}^k denote the *Christoffel symbols*, and we set

$$\alpha(0) = \theta^* \quad \text{and} \quad \dot{\alpha}(0) = \mathbf{v} \sim q(\mathbf{v}|\mathcal{D}) \quad (15)$$

as the initial conditions. A sample from the Riemannian approximate posterior is then obtained by evaluating at $t = 1$, hence $\theta_{\text{R}}^s = \alpha(1)$. This is equivalent to computing the *exponential map* followed by a projection to the parameter space, i.e. $(\theta_{\text{R}}^s, \mathcal{L}(\theta_{\text{R}}^s)) = \text{Exp}_{h(\theta^*)}(\mathbf{J}_h(\theta^*)\mathbf{v})$.

It should be noted that the Christoffel symbols depend on the choice of metric. We equip \mathcal{M} with the *pullback* metric as follows. For two vectors $\mathbf{u}_1, \mathbf{u}_2 \in \Theta$, we evaluate the scalar product at $h(\theta) \in \mathcal{M}$ by computing

$$\langle \mathbf{u}_1, \mathbf{u}_2 \rangle_{\mathbf{G}(\theta)} = (\mathbf{J}_h(\theta)\mathbf{u}_1)^{\top} (\mathbf{J}_h(\theta)\mathbf{u}_2) \quad (16)$$

$$= \underbrace{\mathbf{u}_1^{\top} \mathbf{J}_h(\theta)^{\top} \mathbf{J}_h(\theta) \mathbf{u}_2}_{=\mathbf{G}(\theta)} \quad (17)$$

where $\mathbf{J}_h(\theta) \in \mathbb{R}^{(K+1) \times K}$ is the Jacobian of h evaluated at θ and the matrix $\mathbf{G}(\theta)$ is given by

$$\mathbf{G}(\theta) = \mathbb{I}_K + \nabla_{\theta} \mathcal{L}(\theta) \nabla_{\theta} \mathcal{L}(\theta)^{\top}. \quad (18)$$

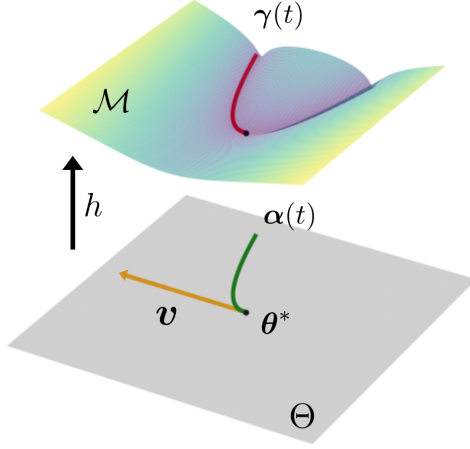


Figure 2. The flat parameter space Θ and a two-dimensional surface $h(\Theta) = \mathcal{M}$. The arrow (—) represents the initial velocity vector v of $\alpha(t)$ (—) at the starting point $\theta^* = \alpha(0)$, that is, $\dot{\alpha}(0) = v$. By mapping $\alpha(t)$ to \mathcal{M} through h , we obtain the corresponding geodesic $\gamma(t) = h(\alpha(t))$ (—) on \mathcal{M} . In this specific example we obtain a geodesic path lying in a low loss region.

Using this metric, the geodesic equation (14) reduces to

$$\ddot{\alpha}(t) = -\frac{\dot{\alpha}(t)^\top \mathbf{H}_{\mathcal{L}}(\alpha(t)) \dot{\alpha}(t)}{1 + \|\nabla_{\theta} \mathcal{L}(\alpha(t))\|^2} \cdot \nabla_{\theta} \mathcal{L}(\alpha(t)), \quad (19)$$

which can be vectorised and computed with automatic differentiation. [Yu et al. \(2024\)](#) choose the Fisher metric, which is less efficient. [Jacobsen et al. \(2026\)](#) take a similar approach in the context of input data augmentation. For further details, we refer to the textbook on differential geometry by [Lee \(2000\)](#) and the lecture notes by [Gudmundsson \(2025\)](#).

3. Riemannian Bayesian Inference in Generative Models

A diffusion-like generative model is by definition not based on a likelihood function. Although the loss objective of such models can be interpreted as a likelihood function if the per-time-step loss terms are sufficiently weighted across time ([Jazbec et al., 2025; Song et al., 2021b](#)), this is generally not the case. For this reason, we consider the Gibbs posterior (or generalised posterior), which replaces the negative log-likelihood in Equation (10) with a (possibly weighted) loss function. In the case of flow matching, this generalised posterior loss function is given by:

$$\tilde{\mathcal{L}}_{\text{post}}(\theta, \mathcal{D}_x) \propto \mathcal{L}_{\text{FM}}(\theta, \mathcal{D}_x) - \log p(\theta). \quad (20)$$

We will consider a uniform prior which is uninformative by definition since $\log p(\theta)$ is constant. Consequently, the generalised posterior loss reduces to the loss function of the generative model. Our Riemannian Bayesian treatment of the generative model then follows a 4-step strategy described in

Algorithm 1 Sampling the Riemannian Laplace Approx.

- 1: **Input:** Generator g_{θ} , data \mathcal{D}_x , base distribution p_0 , parametrisation h of manifold \mathcal{M}
- 2: **Output:** Samples \hat{x}
- 3: **Step 1:** Find the MAP estimate

$$\theta^* = \arg \min_{\theta} \mathcal{L}(\theta, \mathcal{D}_x)$$
- 4: **Step 2:** Compute (or approximate) the Hessian at θ^*

$$\mathbf{H}_{\mathcal{L}}(\theta^*) = \nabla_{\theta}^2 \mathcal{L}(\theta^*)$$
- 5: **Step 3:** Sample initial velocity and map to \mathcal{M} by

$$v \sim \mathcal{N}(\mathbf{0}, \mathbf{H}_{\mathcal{L}}^{-1}(\theta^*))$$

$$(\theta_{\text{R}}^s, \mathcal{L}(\theta_{\text{R}}^s)) = \text{Exp}_{h(\theta^*)}(\mathbf{J}_h(\theta^*)v)$$
- 6: **Step 4:** Generate new data using perturbed parameters

$$x_0 \sim p_0, \quad \hat{x} = g_{\theta_{\text{R}}^s}(x_0)$$

Algorithm 1. In contrast, the classic (non-Bayesian) generative model only follows Step 1 and Step 4. We provide a full algorithmic overview for large-scale experiments in Algorithm 2 in Appendix D. Note that we perturb the generator’s parameters *before* carrying out its sampling process.

3.1. Exact Likelihood and Generative Uncertainty

The induced distribution of generated samples is the push-forward of the base distribution p_0 . If the generator g_{θ} is invertible and deterministic for a fixed θ – which is the case for flow matching – we can further leverage the change-of-variables formula. This gives the explicit density:

$$p(\hat{x}|\theta) = p_0(g_{\theta}^{-1}(\hat{x})) \cdot |\det \mathbf{J}_{g_{\theta}^{-1}}(\hat{x})|. \quad (21)$$

Note that this construction allows us to directly compute the likelihood of a data point according to the learnt generator. Hence, we can express the full distribution of generated samples by marginalising over the Riemannian posterior:

$$p(\hat{x}|\mathcal{D}_x) = \mathbb{E}_{q_{\mathcal{M}}(\theta|\mathcal{D}_x)} [p(\hat{x}|\theta)]. \quad (22)$$

This is known as the *posterior predictive distribution* and is well known in predictive modelling, as it forms a posterior distribution over functions rather than parameters. Measuring its variability, e.g. by using the entropy measure, provides a way to quantify uncertainty of the model.

[Jazbec et al. \(2025\)](#) leverage this construction for generative models to propose the concept of *generative uncertainty*. They formulate a semantic likelihood by encoding generated images to a semantic latent space (such as CLIP) and then placing a Gaussian distribution over the sample. Our formulation of the likelihood of a generated image in Equation (21) requires no such construction and can be directly computed, using only the generative model itself.

4. Theoretical Insights

In this section we prove that parameter perturbations can reduce memorisation. We argue that this is due to the resulting changes of the learnt velocity field, and thus the generated data samples. We further show that the Riemannian method achieves better generalisation than its Euclidean counterpart.

4.1. How Perturbations Impact the Vector Field

The parameter space perturbations induce new vector fields. For a fixed initial value, we analyse the trajectories and endpoints of a particle subject to these new vector fields. For the classic Laplace, there is a bias. For small perturbations, and assuming that u_{θ} is sufficiently smooth for all (x, t) in our domain of interest, we can use a Taylor approximation:

$$u_{\theta_E^s}(x(t), t) \approx u_{\theta^*}(x(t), t) + (\theta^s - \theta^*)^\top \nabla_{\theta} u_{\theta^*}(x(t), t). \quad (23)$$

Plugging this into Equation (2), and using that $\theta_E^s - \theta^* = v \sim \mathcal{N}(\mathbf{0}, \Sigma)$, this induces a *random ODE*:

$$\begin{aligned} x(0, v) &= x_0, \\ \dot{x}(t, v) &= u_{\theta^*}(x(t, v), t) + v^\top \nabla_{\theta} u_{\theta^*}(x(t, v), t). \end{aligned} \quad (24)$$

Due to the dependence on v , we will denote the perturbed paths as $x(t, v)$. Each such random vector field as in Equation (24) now induces a generator g_{θ^*+v} , which takes initial values $x_0 \sim p_0$ to some \hat{x} . Thus, $g_{\theta^*}(x_0)$ is the endpoint of the unperturbed trajectory.

Assuming that for a fixed initial value x_0 the mapping

$$\varphi_{x_0} : \Theta \rightarrow \mathcal{X}, \quad \varphi_{x_0}(v) = g_{\theta^*+v}(x_0)$$

is smooth in v , we may write:

$$\varphi_{x_0}(v) \approx g_{\theta^*}(x_0) + v^\top \frac{\partial \varphi_{x_0}(v)}{\partial v} \Big|_{v=0} + \frac{1}{2} v^\top \frac{\partial^2 \varphi_{x_0}(v)}{\partial v^2} \Big|_{v=0} v.$$

Thus, depending on these sensitivities, parameter perturbations can lead to perturbations of generated samples. Consider the various endpoints of perturbed trajectories for a fixed starting point x_0 , we have that

$$\begin{aligned} \mathbb{E}_{q(v)} [\varphi_{x_0}(v)] &= g_{\theta^*}(x_0) + \frac{1}{2} \mathbb{E}_{q(v)} \left[v^\top \frac{\partial^2 \varphi_{x_0}(v)}{\partial v^2} \Big|_{v=0} v \right], \\ \text{Var}_{q(v)} [\varphi_{x_0}(v)] &= \mathbb{E}_{q(v)} \left[\frac{\partial \varphi_{x_0}(v)}{\partial v} \Big|_{v=0} \Sigma \frac{\partial \varphi_{x_0}(v)}{\partial v} \Big|_{v=0}^\top \right]. \end{aligned}$$

This shows that parameter perturbations can be biased and their variance depends on $\Sigma = \mathbf{H}_{\mathcal{L}}^{-1}(\theta^*)$.

4.2. Why Perturbations Help Mitigate Memorisation

We show that points that are on the edge of being memorised can gain sufficient distance from the training samples to be

reclassified as not memorised. In the previous section we have shown that the perturbed parameters induce different vector fields. Hence, we expect that for some initial values we obtain different endpoints. Let x_0 be such an initial value, θ^* the MAP estimate and θ' the perturbed parameter. Suppose they induce the generators g_{θ} and $g_{\theta'}$ such that

$$\hat{x}' = g_{\theta'}(x_0) \neq g_{\theta}(x_0) = \hat{x}.$$

We write $\delta = \hat{x}' - \hat{x}$ to denote the displacement vector between the two generated points. We will show that perturbations are most influential for data points that are close to the memorisation boundary: if a point \hat{x} is clearly memorised, or clearly not memorised, this is unlikely to change under perturbations. However, points that are only narrowly classified as memorised might get pushed away from the closest training point $x^{(1)}(\hat{x})$ after a small perturbation of the vector field. This can be illustrated in a simplified case.

Theorem 4.1. *Let \hat{x} be memorised, i.e. $\|\hat{x} - x^{(1)}(\hat{x})\|^2 \leq c\|\hat{x} - x^{(2)}(\hat{x})\|^2$. Suppose that the perturbed point $\hat{x}' = \hat{x} + \delta$ wanders away from $x^{(1)}(\hat{x})$, and straight towards $x^{(2)}(\hat{x})$. Then, \hat{x}' is not memorised only if*

$$\begin{aligned} \|\delta\|(1 + \sqrt{c}) &< \|\hat{x} - x^{(2)}(\hat{x})\| - \sqrt{c}\|\hat{x} - x^{(1)}(\hat{x})\|, \\ \|\delta\|(1 + \sqrt{c}) &> \sqrt{c}\|\hat{x} - x^{(2)}(\hat{x})\| - \|\hat{x} - x^{(1)}(\hat{x})\|. \end{aligned}$$

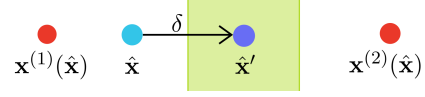


Figure 3. In the setting of Theorem 4.1, in which all considered points lie on one straight line, the perturbation makes a generated point (blue) wander straight towards the second closest training sample (red). If the new point (blue) falls into the green zone, it is no longer classified as memorised. The size of the green zone depends on $\|\hat{x} - x^{(1)}(\hat{x})\| + \|\hat{x} - x^{(2)}(\hat{x})\|$, and is maximised if \hat{x} is right between the two training samples.

For the proof, see Appendix B. Due to its strong assumptions, this argument is not intended to be quantitatively predictive, but it provides a useful qualitative explanation of why perturbations mitigate memorisation.

4.3. Analysis of the Riemannian Paths

Although perturbing the model's parameters can mitigate memorisation, it comes with the risk of deteriorating its generalisation capabilities. We show that samples from our Riemannian Laplace preserve generalisation better than its Euclidean counterpart, since the perturbed parameters stay in low loss regions. It is evident that the Euclidean perturbation upper bounds the Riemannian, as it moves in a straight line, which is the shortest path in the flat parameter space. The Riemannian sample follows a different path, which cannot lead further away than the straight line.

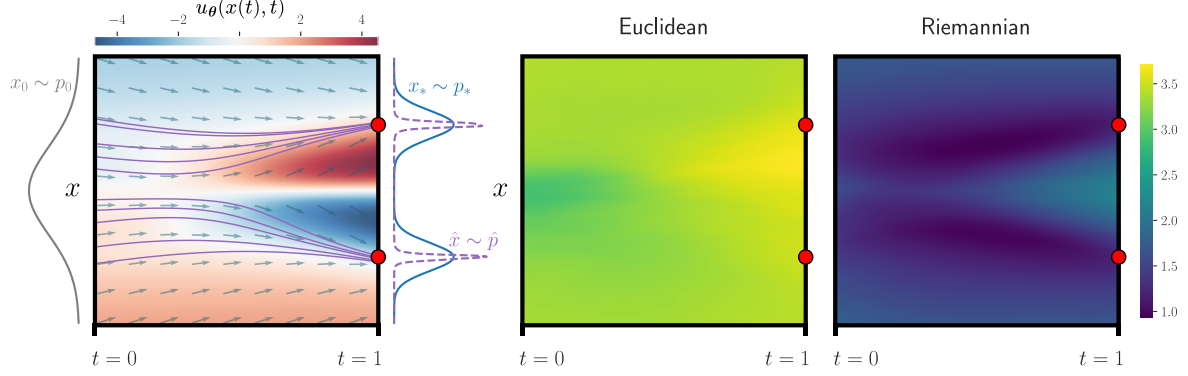


Figure 4. A 1D flow matching toy problem with a Gaussian base distribution p_0 and a GMM as the target distribution p_* . *Left:* the learnt conditional vector field $u_\theta(x(t), t) : \mathbb{R} \times [0, 1] \rightarrow \mathbb{R}$ at the optimal parameters θ^* for $x(t) \in [-3, 3]$ and $t \in [0, 1]$. Each line (—) is a trajectory $x(t)$ of a noise sample $x_0 \sim p_0$ under u_{θ^*} , which yields $x(1) = \hat{x} \sim p(\hat{x})$. This distribution overfits to the two fixed training points (●), hence the generative model g_{θ^*} has learnt to *memorise* rather than generalise to p_* . *Right:* we draw $S = 1000$ models $\theta^s \sim q(\theta|\mathcal{D})$ from the Euclidean and Riemannian approximate posterior. Each model θ^s gives a specific velocity field (as in *left*). We show the standard deviation per $(x(t), t)$ -coordinate computed over the S different velocity fields.

Theorem 4.2. *Following the constructions in Subsection 2.2.1, we have that $\|\theta_E^s - \theta^*\| \geq \|\theta_R^s - \theta^*\|$.*

For the proof, see Appendix B.2. Computation B.3 in the Appendix approximates the curve $\alpha(t)$ using n Euler steps of size $\epsilon = 1/n$, and allows us to estimate $\alpha(1)$ for sufficiently small ϵ .

$$\theta_R^s = \alpha(1) \approx \theta_E^s + \epsilon^2 \sum_{j=0}^{n-2} (n-1-j) \ddot{\alpha}(j\epsilon). \quad (25)$$

Combining Equations (19), (23) and (25), we obtain

$$u_{\theta_R^s}(x(t), t) \approx u_{\theta_E^s}(x(t), t) - \epsilon^2 \kappa^\top \nabla_\theta u_{\theta^*}(x(t), t) \quad (26)$$

where the correction vector κ is given by

$$\kappa = \sum_{j=0}^{n-2} (n-1-j) \frac{\dot{\alpha}(j\epsilon)^\top \mathbf{H}_\mathcal{L}(\alpha(j\epsilon)) \dot{\alpha}(j\epsilon)}{1 + \|\nabla_\theta \mathcal{L}(\alpha(j\epsilon))\|^2} \nabla_\theta \mathcal{L}(\alpha(j\epsilon)).$$

This lets us compare how the Riemannian and Euclidean perturbations impact the vector field. The second term in Equation (26) opposes motion into directions of rapidly increasing loss. If $\dot{\alpha}(t)$ is aligned with directions where the loss increases sharply, then the correction term is of large magnitude. Specifically, if $\dot{\alpha}(t)$ points in the direction of the top-eigenvector of the Hessian, the difference between the straight (Euclidean) and geodesic (Riemannian) paths in the parameter space will be maximised. If however $\dot{\alpha}(t)$ points in directions where the loss is flat, the Euclidean and Riemannian vector fields will be close. Thus, the Riemannian method shrinks steps toward this direction, and helps us to stay in parameter regions with lower loss.

5. Experiments

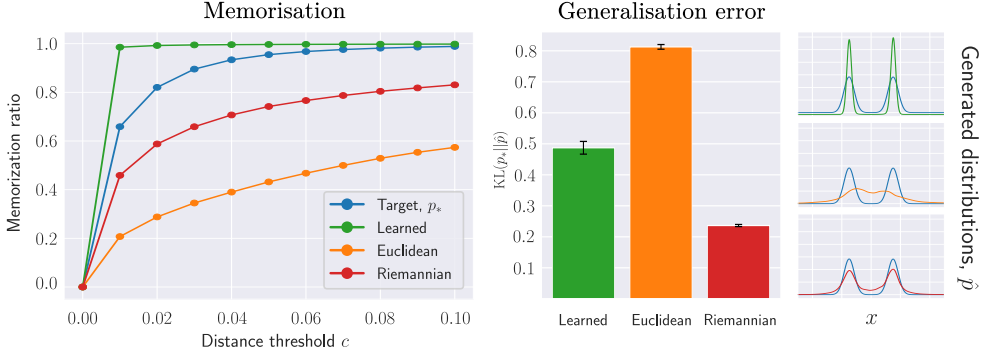
5.1. Toy Experiments

We first consider the problem of learning a flow matching model in D dimensions with the base distribution being an isotropic Gaussian, $p_0 \sim \mathcal{N}(\mathbf{0}, \mathbb{I}_D)$, and the target distribution p_* being a Gaussian mixture model (GMM). See Appendix C for details on the setup, and results for $D = 2$.

1D: For $D = 1$, we define the target distribution to have means $\{\mu_1, \mu_2\} = \{-1.5, 1.5\}$ and variances $\sigma_1^2 = \sigma_2^2 = 0.1$. For learning a generative model that *memorises* (i.e. overfits), we construct a naively simple training set that consists of only 2 points: μ_1 and μ_2 . We show the learning problem and the overfitted velocity field in Figure 4 (*left*).

We adopt a Riemannian Bayesian treatment of the model parameters following Section 2.2. We then define the distributions of generated data samples under the two approximate posteriors as in Equation (22) by sampling $S = 1000$ samples from the posterior $\theta^s \sim q(\theta|\mathcal{D}_x)$ and $N = 1000$ samples from the base distribution $x_0 \sim p_0$. Note that each posterior sample induces a different velocity field.

Figure 4 (*right*) shows the uncertainty at each (x_t, t) -coordinate, computed as the standard deviation over the S posterior samples. Notably, the velocity fields induced by the Riemannian samples are far less uncertain than the Euclidean ones, especially along the path where the original vector field has low magnitude. This is also seen in the symmetry patterns: the learnt vector field is an odd function in x , while the Riemannian uncertainty is even, suggesting that velocity fields associated to perturbations from the Riemannian posterior still respect the symmetry of the original model. The Euclidean heat map has no such symmetry.



We provide the memorisation and generalisation capabilities in Figure 5 and see that perturbing the model parameters reduces memorisation, no matter the choice of distance threshold c . This supports our argument in Subsection 4.2. Although the generated samples using Euclidean perturbations exhibit less memorisation than the Riemannian ones, this comes at the cost of poorer generalisation, measured as the alignment with the underlying target distribution.

5.2. CIFAR-10

We also apply our strategy to an unconditional diffusion model based on a U-Net architecture with roughly 36B parameters. As argued by Gu et al. (2025), training on large amounts of training data results in limited to no memorisation. Therefore, we train a diffusion model on a subset of $N = 1000$ training samples from CIFAR-10 (Krizhevsky et al., 2009), yielding the MAP θ^* . For computational reasons, we restrict our Bayesian treatment to be on a subset of the parameters, specifically the parameters of the first layer. Note that this construction serves as a proof-of-concept for applying our technique to high-dimensional settings, and that this approximate posterior does not capture the full flexibility of our approach.

Next, we approximate the Hessian at the MAP, noting that its spectrum is dominated by a few large eigenvalues, with most others being near zero (as also observed by Roy et al. (2024)). This indicates that only certain directions in the parameter space strongly influence the loss, and that it remains relatively flat along most other directions. Consequently, Riemannian perturbations differ from Euclidean ones mainly along the top-eigenvectors directions.

We conduct a structured experiment by sampling along the most curved direction as well as the direction of the lowest



Figure 6. Generated images with the MAP model (top) and under Riemannian perturbations along the eigenvectors with highest and lowest positive eigenvalues (middle and bottom row). For each column, we use a fixed initial value $\mathbf{x}_0 \sim p_0$. Along the bottom-eigenvector, the parameter space is flatter, and the generated images are close to the MAP generator's images. Images generated under perturbation by the top-eigenvector tend to converge to a few specific images: for three distinct \mathbf{x}_0 , we obtain the same deer.

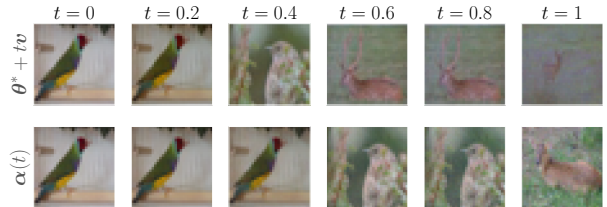


Figure 7. How a sample from a generative model changes when gradually perturbing the parameters along the path induced by the top-eigenvector. We fix the noise sample \mathbf{x}_0 for all images. Top: along the straight path $\theta^* + tv$. Bottom: along the curve $\alpha(t)$.

positive eigenvalue, rather than using the full inverse Hessian as the Laplace covariance. In Figure 6, we show the generated images when following the Riemannian perturbation technique with these eigenvectors as the initial velocities. While images generated using the bottom-eigenvector perturbation are identical or qualitatively close to the images generated with the MAP model, images generated with the top-eigenvector are visually very different, yet result in a similarly looking image for all considered base distribution

samples. This indicates that the resulting vector field is a sink: there exists one dominant point \hat{x} , such that all nearby paths converge towards it. Understanding this behaviour and how to avoid it constitutes future work.

In Figure 7, we experimentally verify the claim from Sub-section 4.3, namely that the Riemannian paths stay closer to well-generalising generators. By again considering the worst-case perturbation along the top-eigenvector, we see that the Euclidean approach yields a generator that ends up in a parameter space location where meaningless images are generated. As expected, the Riemannian paths favour low-loss regions, conserving a high image quality.

Although our method is not optimised for the image domain, we show that the parameters of complex generators can be manipulated in a controlled way. Further implications and connections to memorisation are discussed in Appendix D.

6. Related Work and Discussion

6.1. What Drives Generalisation?

At present, it remains unresolved whether diffusion models truly generalise at all, and if so, how and why. Kadkhodaie et al. (2023) demonstrate empirically that large datasets are necessary to generalise, as they allow diffusion models to recover a geometry-aligned score function. Another promising line of work reveals that the amount of memorisation in generative models increases with training time and is inversely proportional to the size of the training set (Gu et al., 2025; Biroli et al., 2024; Bonnaire et al., 2025). In contrast, our work focuses on reducing memorisation after the generative model is already fully trained. We do so by investigating how to represent uncertainty and preserve generalisation around the learnt model, independent of further increases in data and training time.

Bertrand et al. (2025) demonstrate that target stochasticity (the randomness of the training target arising from the sampling process) is not driving generalisation – in fact, there exists a closed form solution for the flow matching loss. Interestingly, this closed form solution only reproduces training samples. They conclude that generalisation occurs precisely when the network *fails* to fit the optimal vector field. Our work, however, introduces stochasticity in the parameter space. By perturbing the optimal vector field, we *deliberately prevent* the collapse to a deterministic flow, and achieve the described generalisation inducing effect.

6.2. Balancing Generalisation and Memorisation.

Our results highlight that reducing memorisation alone does not guarantee improved generalisation; rather, we observe a delicate trade-off between memorisation and generalisation. The Euclidean method exhibits the least memorisation,

since the parameter perturbations encourage a broader variance over the output space. However, this comes at the cost of poorer generalisation, demonstrating that counteracting memorisation too aggressively can prevent the model from learning meaningful structures. The Riemannian method, on the other hand, provides a good balance: it still exhibits less memorisation than the baseline, while achieving substantially stronger generalisation.

6.3. How Should We Measure Memorisation?

The nearest neighbours memorisation ratio defined in Equation (8) is easy to evaluate, however a downside is the dependence on Euclidean distance, which does not take the structure of the data manifold into account and therefore does not necessarily align with semantic similarity in the data domain. In the case of image data, previous work (Pizzi et al., 2022; Chen et al., 2024) considers embedding the generated images and training images to a semantic latent space using a pre-trained encoder, e.g. trained using self-supervised learning. A different line of research (Khrulkov et al., 2020; Atigh et al., 2022) embeds image data into the hyperbolic space instead. Hyperbolic manifolds have a negative curvature and are thus better at representing hierarchical data with minimal distortion. In the image domain, visual concepts can induce a hierarchy (for example, felines and canines have distinct shapes), but we can also consider a hierarchy based on information content or degradation.

Further, the constant c is somewhat arbitrary: in the image domain, for example, it is often set to $c = \frac{1}{3}$ since this value has been found to work well empirically on the considered data sets. In the future, we hope to see a theory-backed rule of choosing an appropriate c for a given data set in a way that aligns with human perception. Lastly, the nearest neighbour memorisation measure suffers from the curse of dimensionality: pairwise distances between samples tend to concentrate as the dimension increases, limiting the interpretability of the measure. We also want to remark that this criterion becomes meaningless in case of duplicate training points, which is the case for CIFAR-10.

Alternative measures for memorisation have been proposed, for example by Ross et al. (2024). Their work compares the local intrinsic dimension (LID) of the ground truth data manifold and of the learnt data manifold. They label a point as memorised if the dimension of the learnt manifold is lower than the dimension of the ground truth manifold. This measure carries a nice geometric flavour and provides more qualitative information about the structure of the learnt distribution than merely evaluating distances between points. However, the estimation of the LID is computationally heavy and harder to evaluate, although improvements have been made by Kamkari et al. (2024). We expect that our method also helps mitigate this notion of memorisation:

if a perturbed vector field leads to a different endpoint, this increases the dimension of the learnt manifold.

7. Conclusion

Our work presents a Bayesian and Riemannian framework for exploring the parameter space of large generative models. Adopting a geometry-informed Bayesian treatment of the model parameters can help reduce memorisation, without loosing generalisation capabilities. This finding is based both on theoretical and empirical foundations: Section 4 provides a mathematical explanation, while Section 5 contains a one-dimensional example, allowing for visually interpreting the effects of our Riemannian Bayesian treatment of the model parameters. We lastly showed that our method scales to settings with high-dimensional parameter spaces.

7.1. Limitations and Future Work

Rather than competing with state-of-the-art image generators, we demonstrated the feasibility of our approach. Although our approximate posterior is flexible, it is inherently mode-based and centred around the MAP solution. In the image domain, the generated data points closely resemble the training data with added unstructured noise, which ideally should be structured to change the image concept. Furthermore, due to computational constraints in large models, we restrict the method to a subset of the parameter space. We expect that specialised geodesic solvers for high-dimensional manifolds could lead to improvements.

Acknowledgments

This work was supported by the Danish Data Science Academy, which is funded by the Novo Nordisk Foundation (NNF21SA0069429) and VILLUM FONDEN (40516), and by the DFF Sapere Aude Starting Grant “GADL” and by the Horizon-EU EIC Pathfinder Open program to i-RASE: Intelligent Radiation Sensor Readout System, with reference number: HE EIC - i-RASE – 101130550. We thank Stas Syrota and Federico Bergamin for early discussions that helped shaping our understanding of the relationship between diffusion and flow matching.

8. Impact Statement

Generative models are increasingly deployed in high-stakes applications, and thus, mitigating memorisation is crucial. We propose a novel perspective on tackling this issue, and as a result, the proposed approach can help mitigate risks associated with memorisation, including the reproduction of sensitive data. The general aim of reducing memorisation in generative models can seem as appealing in order to avoid copyright infringement issues. However, as the underlying

process becomes less transparent, it becomes harder for e.g. independent artists to prove such violations.

Beyond these considerations, our work contributes to the broader goal of building more reliable and robust generative models, and better understanding their underlying mechanisms.

References

Mina Ghadimi Atigh, Julian Schoep, Erman Acar, Nanne Van Noord, and Pascal Mettes. Hyperbolic image segmentation. In *Proceedings of the IEEE/CVF conference on computer vision and pattern recognition*, pages 4453–4462, 2022.

Federico Bergamin, Pablo Moreno-Muñoz, Søren Hauberg, and Georgios Arvanitidis. Riemannian Laplace approximations for Bayesian neural networks. *Neural Information Processing Systems (NeurIPS)*, 2023.

Quentin Bertrand, Anne Gagneux, Mathurin Massias, and Rémi Emonet. On the closed-form of flow matching: Generalization does not arise from target stochasticity. *Neural Information Processing Systems (NeurIPS)*, 2025.

Giulio Biroli, Tony Bonnaire, Valentin De Bortoli, and Marc Mézard. Dynamical regimes of diffusion models. *Nature Communications*, 15(1):9957, 2024.

Tony Bonnaire, Raphaël Urfin, Giulio Biroli, and Marc Mézard. Why diffusion models don’t memorize: The role of implicit dynamical regularization in training. *Neural Information Processing Systems (NeurIPS)*, 2025.

Sam Buchanan, Druv Pai, Yi Ma, and Valentin De Bortoli. On the edge of memorization in diffusion models. *Neural Information Processing Systems (NeurIPS)*, 2025.

Chen Chen, Daochang Liu, and Chang Xu. Towards memorization-free diffusion models. In *Proceedings of the IEEE/CVF Conference on Computer Vision and Pattern Recognition*, pages 8425–8434, 2024.

John R. Dormand and Peter J. Prince. A family of embedded Runge-Kutta formulae. *Journal of computational and applied mathematics*, 6(1):19–26, 1980.

Ruiqi Gao, Emiel Hoogeboom, Jonathan Heek, Valentin De Bortoli, Kevin P. Murphy, and Tim Salimans. Diffusion meets flow matching: Two sides of the same coin. 2024. URL <https://diffusionflow.github.io/>.

Xiangming Gu, Chao Du, Tianyu Pang, Chongxuan Li, Min Lin, and Ye Wang. On memorization in diffusion models. *Transactions on Machine Learning Research (TMLR)*, 2025.

Sigmundur Gudmundsson. *An Introduction to Riemannian Geometry*. 2025. URL <https://www.matematik.lu.se/matematiklu/personal/sigma/Riemann.pdf>.

Marcelo Hartmann, Mark Girolami, and Arto Klami. Lagrangian manifold Monte Carlo on Monge patches. *International Conference on Artificial Intelligence and Statistics*, 2022.

Martin Heusel, Hubert Ramsauer, Thomas Unterthiner, Bernhard Nessler, and Sepp Hochreiter. Gans trained by a two time-scale update rule converge to a local nash equilibrium. *Advances in neural information processing systems*, 30, 2017.

Jonathan Ho, Ajay Jain, and Pieter Abbeel. Denoising diffusion probabilistic models. *Neural Information Processing Systems (NeurIPS)*, 2020.

Peter Holderrieth and Ezra Erives. Introduction to flow matching and diffusion models, 2025. URL <https://diffusion.csail.mit.edu/>.

Albert Kjøller Jacobsen and Georgios Arvanitidis. Monge SAM: Robust reparameterization-invariant sharpness-aware minimization based on loss geometry. *arXiv:2502.08448*, 2025.

Albert Kjøller Jacobsen, Johanna Marie Gegenfurtner, and Georgios Arvanitidis. Staying on the manifold: Geometry-aware noise injection. *Northern Lights Deep Learning Conference (NLDL)*, 2026.

Metod Jazbec, Eliot Wong-Toi, Guoxuan Xia, Dan Zhang, Eric Nalisnick, and Stephan Mandt. Generative uncertainty in diffusion models. *Uncertainty in Artificial Intelligence (UAI)*, 2025.

Zahra Kadkhodaie, Florentin Guth, Eero P Simoncelli, and Stéphane Mallat. Generalization in diffusion models arises from geometry-adaptive harmonic representations. *arXiv preprint arXiv:2310.02557*, 2023.

Hamidreza Kamkari, Brendan Leigh Ross, Rasa Hosseinzadeh, Jesse C. Cresswell, and Gabriel Loaiza-Ganem. A geometric view of data complexity: Efficient local intrinsic dimension estimation with diffusion models. *arXiv:2406.03537*, 2024.

Valentin Khrulkov, Leyla Mirvakhabova, Evgeniya Ustanova, Ivan Oseledets, and Victor Lempitsky. Hyperbolic image embeddings. In *Proceedings of the IEEE/CVF conference on computer vision and pattern recognition*, pages 6418–6428, 2020.

Alex Krizhevsky, Geoffrey Hinton, et al. Learning multiple layers of features from tiny images. 2009. URL <https://www.cs.utoronto.ca/~kriz/learning-features-2009-TR.pdf>.

Cornelius Lanczos. An iteration method for the solution of the eigenvalue problem of linear differential and integral operators. *Journal of research of the National Bureau of Standards*, 45(4):255–282, 1950.

John M. Lee. *Introduction to Smooth Manifolds*. Springer New York, 2000.

Yihao Liu, Jinhe Huang, Yanjie Li, Dong Wang, and Bin Xiao. Generative ai model privacy: a survey. *Artificial Intelligence Review*, 58(1):33, 2024.

Gabriel Peyré, Marco Cuturi, et al. Computational optimal transport: With applications to data science. *Foundations and Trends® in Machine Learning*, 11(5-6):355–607, 2019.

Ed Pizzi, Sreya Dutta Roy, Sugosh Nagavara Ravindra, Priya Goyal, and Matthijs Douze. A self-supervised descriptor for image copy detection. In *Proceedings of the IEEE/CVF Conference on Computer Vision and Pattern Recognition*, pages 14532–14542, 2022.

Brendan Leigh Ross, Hamidreza Kamkari, Tongzi Wu, Rasa Hosseinzadeh, Zhaoyan Liu, George Stein, Jesse C Cresswell, and Gabriel Loaiza-Ganem. A geometric framework for understanding memorization in generative models. *Neural Information Processing Systems (NeurIPS)*, 2024.

Hritik Roy, Marco Miani, Carl Henrik Ek, Philipp Henning, Marvin Pförtner, Lukas Tatzel, and Søren Hauberg. Reparameterization invariance in approximate bayesian inference. *Advances in Neural Information Processing Systems*, 37:8132–8164, 2024.

Samuel L Smith, Benoit Dherin, David GT Barrett, and Soham De. On the origin of implicit regularization in stochastic gradient descent. *arXiv preprint arXiv:2101.12176*, 2021.

Jascha Sohl-Dickstein, Eric A. Weiss, Niru Maheswaranathan, and Surya Ganguli. Deep unsupervised learning using nonequilibrium thermodynamics. *arXiv:1503.03585*, 2015.

Jiaming Song, Chenlin Meng, and Stefano Ermon. Denoising diffusion implicit models. In *International Conference on Learning Representations (ICLR)*, 2021a.

Yang Song, Conor Durkan, Iain Murray, and Stefano Ermon. Maximum likelihood training of score-based diffusion models. *Advances in neural information processing systems*, 34:1415–1428, 2021b.

Cédric Villani et al. *Optimal transport: old and new*, volume 338. Springer, 2008.

Bernardo Williams, Hanlin Yu, Hoang Phuc Hau Luu, Georgios Arvanitidis, and Arto Klami. Geodesic slice sampler for multimodal distributions with strong curvature. *Uncertainty in Artificial Intelligence (UAI)*, 2025.

TaeHo Yoon, Joo Young Choi, Sehyun Kwon, and Ernest K Ryu. Diffusion probabilistic models generalize when they fail to memorize. In *ICML 2023 workshop on structured probabilistic inference & generative modeling*, 2023.

Hanlin Yu, Marcelo Hartmann, Bernardo Williams, Mark Girolami, and Arto Klami. Riemannian Laplace approximation with the Fisher metric. *International Conference on Artificial Intelligence and Statistics (AISTATS)*, 2024.

A. Essential Facts on Geodesics

In this section, we will explain a few concepts we use when constructing the Riemannian Laplace approximation 2.2.1.

The Christoffel symbols describe how much basis vectors evolve along a manifold, and are useful for computations, including the geodesic equation (14). We have the following formal definition.

Definition A.1. (Gudmundsson, 2025) Let (\mathcal{M}, g) be a Riemannian manifold with Levi-Civita connection ∇ . Further let (U, x) be a local chart on \mathcal{M} and put $X_i = \frac{\partial}{\partial x_i} \in \mathcal{C}^\infty(TU)$, so that $\{X_1, \dots, X_m\}$ is a local frame for $T\mathcal{M}$ on U . Then we define the Christoffel symbols $\Gamma_{ij}^k : U \rightarrow \mathbb{R}$ of the connection ∇ with respect to (U, x) by

$$\nabla_{X_i} X_j = \sum_{k=1}^m \Gamma_{ij}^k \cdot X_k.$$

Let \mathbf{G} denote the matrix form of the metric g , that is $\mathbf{G}_{ij} = g(X_i, X_j)$. Then, Γ_{ij}^k is given by

$$\Gamma_{ij}^k = \frac{1}{2} \sum_{l=1}^m (\mathbf{G}^{-1})_{kl} \left\{ \frac{\partial \mathbf{G}_{jl}}{\partial x_i} + \frac{\partial \mathbf{G}_{li}}{\partial x_j} - \frac{\partial \mathbf{G}_{ij}}{\partial x_l} \right\}.$$

This formula lets us compute the Christoffel symbols easily.

We also mention the exponential map. It essentially wraps the tangent space at a given point around the manifold. In two dimensions this is easy to picture: take an apple or a bagel, whose surfaces can be approximated by a sphere or a torus, respectively. If you stick aluminium foil to one particular point, you will be able to smoothly fit a small patch of the foil around the point without it wrinkling or tearing. Similarly, the exponential map takes vectors from a subset of the tangent space at the chosen point and maps them to the manifold, specifically by evaluating the geodesics with the given initial velocity.

Definition A.2. (Gudmundsson, 2025) Let (\mathcal{M}, g) be an m -dimensional Riemannian manifold, $p \in \mathcal{M}$ and

$$S_p^{m-1} = \{\mathbf{v} \in T_p \mathcal{M} \mid g_p(\mathbf{v}, \mathbf{v}) = 1\}.$$

For every $\mathbf{v} \in S_p^{m-1}$ let $\gamma_{\mathbf{v}} : (-a_{\mathbf{v}}, b_{\mathbf{v}}) \rightarrow \mathcal{M}$ be the maximal geodesic such that $a_{\mathbf{v}}, b_{\mathbf{v}} \in \mathbb{R}^+$, $\gamma(0) = p$, and $\dot{\gamma}(0) = \mathbf{v}$. It can be shown that $\epsilon_p = \inf\{a_{\mathbf{v}}, b_{\mathbf{v}} \mid \mathbf{v} \in S_p^{m-1}\}$ is positive, and thus the open ball

$$\mathcal{B}_{\epsilon_p}^m(0) = \{\mathbf{v} \in T_p \mathcal{M} \mid g_p(\mathbf{v}, \mathbf{v}) < \epsilon_p\}$$

is non-empty. The exponential map $\text{Exp}_p : \mathcal{B}_{\epsilon_p}^m(0) \rightarrow \mathcal{M}$ at p is given by

$$\text{Exp}_p(\mathbf{v}) = \begin{cases} \gamma_{\frac{\mathbf{v}}{\|\mathbf{v}\|}}(\|\mathbf{v}\|) & \text{if } \mathbf{v} \in \mathcal{B}_{\epsilon_p}^m(0) \setminus \{\mathbf{0}\}, \\ p & \text{if } \mathbf{v} = \mathbf{0}. \end{cases} \quad (27)$$

B. Details from the Theory Section

B.1. Proof of Theorem 4.1

Proof. We assume that $\hat{\mathbf{x}}$ and $\mathbf{x}' = \hat{\mathbf{x}} + \delta$ lie on the straight line between $\mathbf{x}^{(1)}(\hat{\mathbf{x}})$ and $\mathbf{x}^{(2)}(\hat{\mathbf{x}})$, such that $\hat{\mathbf{x}}$ is closer to $\mathbf{x}^{(1)}(\hat{\mathbf{x}})$ than \mathbf{x}' is. Hence, we have that

$$\|\hat{\mathbf{x}}' - \mathbf{x}^{(1)}(\hat{\mathbf{x}})\| = \|\hat{\mathbf{x}} - \mathbf{x}^{(1)}(\hat{\mathbf{x}})\| + \|\delta\|, \quad (28)$$

$$\|\hat{\mathbf{x}}' - \mathbf{x}^{(2)}(\hat{\mathbf{x}})\| = \|\hat{\mathbf{x}} - \mathbf{x}^{(2)}(\hat{\mathbf{x}})\| - \|\delta\|. \quad (29)$$

For $\hat{\mathbf{x}}'$ to not be memorised, it cannot be too close to either $\mathbf{x}^{(1)}(\hat{\mathbf{x}})$ or $\mathbf{x}^{(2)}(\hat{\mathbf{x}})$. Specifically, we need

$$\|\hat{\mathbf{x}}' - \mathbf{x}^{(1)}(\hat{\mathbf{x}})\| > \sqrt{c} \|\hat{\mathbf{x}}' - \mathbf{x}^{(2)}(\hat{\mathbf{x}})\|, \quad (30)$$

$$\|\hat{\mathbf{x}}' - \mathbf{x}^{(2)}(\hat{\mathbf{x}})\| > \sqrt{c} \|\hat{\mathbf{x}}' - \mathbf{x}^{(1)}(\hat{\mathbf{x}})\|^2. \quad (31)$$

Plugging now Equations (28) and (29) into (30) and (31), and moving terms around, we obtain the desired bound. \square

B.2. Comparing Displacement Under the Riemannian and Euclidean Perturbation.

We will provide a standard argument which shows that $\|\theta_E^s - \theta^*\| \geq \|\theta_R^s - \theta^*\|$.

Proof. Recall that geodesics have unit speed, hence

$$\|\dot{\gamma}(t)\| \equiv \|\dot{\gamma}(0)\| = \|\mathbf{J}_h(\theta^*)\mathbf{v}\|.$$

Since θ^* minimises $\mathcal{L}(\theta)$, we have that $\mathbf{J}_h(\theta^*) = [\mathbb{I}_K \quad \mathbf{0}]^\top$. Thus, $\|\dot{\gamma}(t)\| \equiv \|\mathbf{v}\|$. It now follows that $\gamma(t)_{[0,1]}$ has arc length $\|\mathbf{v}\|$:

$$\int_0^1 \|\dot{\gamma}(t)\| dt = \int_0^1 \|\mathbf{v}\| dt = \|\mathbf{v}\|.$$

Using the definition of $\mathbf{G}(\theta)$ from Equation (18), we now observe that

$$\|\dot{\alpha}(t)\|_{\mathbf{G}(\theta)}^2 \equiv \|\dot{\alpha}(t)\|^2 + \underbrace{\dot{\alpha}(t)^\top \nabla_\theta \mathcal{L}(\theta) \nabla_\theta \mathcal{L}(\theta)^\top \dot{\alpha}(t)}_{\geq 0},$$

and consequently $\|\dot{\alpha}(t)\| \leq \|\dot{\alpha}(t)\|_{\mathbf{G}(\theta)}$. We now evaluate the arc length of $\alpha(t)_{[0,1]}$:

$$\int_0^1 \|\dot{\alpha}(t)\| dt \leq \int_0^1 \|\dot{\alpha}(t)\|_{\mathbf{G}(\theta)} dt = \int_0^1 \|\dot{\gamma}(t)\| dt = \|\mathbf{v}\|,$$

with equality if and only if $\alpha(t)$ is a straight line. As straight lines are the shortest paths in the flat Euclidean space, $\alpha(1) = \theta_R^s$ cannot be further away from θ^* than $\theta^* + \mathbf{v} = \theta_E^s$. \square

B.3. Approximation of the Curve

Assume $\alpha(t) : [0, 1] \subseteq \mathbb{R} \rightarrow \Theta$ is a smooth curve in Θ . We wish to approximate $\alpha(1)$.

We choose $n \in \mathbb{N}_{>0}$, and take discrete time steps of size $\epsilon = \frac{1}{n}$. At each point in time t , we take a step in the direction of $\dot{\alpha}(t)$, and thus

$$\alpha(t + \epsilon) \approx \alpha(t) + \epsilon \dot{\alpha}(t). \quad (32)$$

After n such steps we obtain

$$\begin{aligned} \alpha(1) &\approx \alpha(0) + \epsilon \dot{\alpha}(0) + \epsilon \dot{\alpha}(\epsilon) + \epsilon \dot{\alpha}(2\epsilon) + \cdots + \epsilon \dot{\alpha}((n-1)\epsilon) \\ &= \alpha(0) + \epsilon \cdot \sum_{j=0}^{n-1} \dot{\alpha}(j\epsilon). \end{aligned}$$

Similar to Equation (32), we can update the second derivatives by letting

$$\ddot{\alpha}(t + \epsilon) \approx \ddot{\alpha}(t) + \epsilon \ddot{\alpha}(t). \quad (33)$$

This yields

$$\alpha(1) \approx \alpha(0) + \epsilon \dot{\alpha}(0) + \epsilon \left(\underbrace{\dot{\alpha}(0) + \epsilon \ddot{\alpha}(0)}_{=\dot{\alpha}(\epsilon)} \right) + \epsilon \left(\underbrace{\dot{\alpha}(\epsilon) + \epsilon \ddot{\alpha}(\epsilon)}_{\dot{\alpha}(2\epsilon)} \right) + \cdots + \epsilon \left(\underbrace{\dot{\alpha}((n-2)\epsilon) + \epsilon \ddot{\alpha}((n-2)\epsilon)}_{\dot{\alpha}((n-1)\epsilon)} \right).$$

We can now apply Equation (33) on all the first derivatives $\dot{\alpha}(j\epsilon)$ for $j \neq 0$ again, and see that in total, $\epsilon \dot{\alpha}(0)$ appears n times. Further, for each $j = 0, \dots, n-2$, the term $\epsilon^2 \ddot{\alpha}(j\epsilon)$ will appear $n-1-j$ times. We finally obtain

$$\alpha(n\epsilon) \approx \alpha(0) + \dot{\alpha}(0) + \epsilon^2 \sum_{j=0}^{n-2} (n-1-j) \ddot{\alpha}(j\epsilon). \quad (34)$$

Our approximation is valid up to $\mathcal{O}(\epsilon^2)$. Equivalent derivations can be found in standard textbooks on ordinary differential equations, and a similar computation is done by Smith et al. (2021).

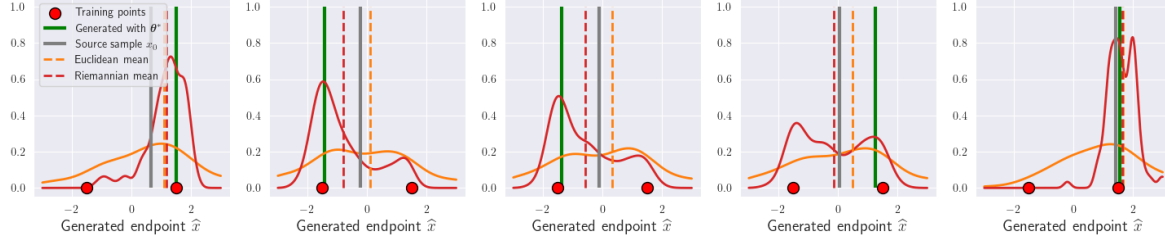


Figure 8. For a fixed initial value x_0 , (—) we plot the distribution of endpoints of the trajectories when following the $S = 1000$ vector fields under the Euclidean Laplace perturbation (—) and the Riemannian Laplace perturbation (—), respectively. The green line (—) demonstrates the endpoint of the original vector field that memorises the training points (●). We use kernel density estimation to visualise the spread of the endpoints. We see that the Euclidean method has a bias and higher variance, whereas the Riemannian method finds the two modes and is often closer to the MAP endpoint.

C. Details of the Toy Experiments

We provide the associated code to all experiments in the repository: github.com/albertkjoller/geometric-ml.

C.1. Toy Experiment in 1D

We adopt a Bayesian treatment of the parameters of u_θ , by defining the likelihood term in Equation (10) as the flow matching loss $\mathcal{L}_{\text{FM}}(\theta)$ and a uniform prior over the weights. This corresponds to placing the Laplace approximation at the maximum likelihood estimate found from training the model with gradient descent. We consider the dataset \mathcal{D} as a fixed collection of data-noise pairings and equidistant time samples, i.e. $\mathcal{D} = \{t_i = \frac{i}{N}, x_0^i, x_*^i\}_{n=1}^N$, for ensuring a deterministic loss.

We sample $S = 1000$ model realisations from the Euclidean approximate posterior $\theta_{\text{E-LA}}^s \sim q(\theta|\mathcal{D})$ and additionally use these as initial velocities for obtaining $S = 1000$ samples from the Riemannian approximate posterior $\theta_{\text{R-LA}}^s \sim q_{\mathcal{M}}(\theta|\mathcal{D})$. For both approximate posterior methods, we compute the velocity field over a space-time grid for each of the model realisations θ_s . We visualise the variation over the associated velocity fields in Figure 4 (right).

Next, we sample $N = 1000$ points from the base distribution and push these through the generator associated to every model realisation. This gives us a set of $N \times S$ generated points for each approximate posterior. We formalise this as:

$$\{\hat{x}_E^i\}_{i=1}^{N \times S} = \{g_{\theta_s}(x_0^i) \mid x_0^i \sim p_0, \theta_s^s \sim q(\theta|\mathcal{D})\}_{i=1,s=1}^{N,S} \quad (35)$$

$$\{\hat{x}_R^i\}_{i=1}^{N \times S} = \{g_{\theta_s}(x_0^i) \mid x_0^i \sim p_0, \theta_R^s \sim q_{\mathcal{M}}(\theta|\mathcal{D})\}_{i=1,s=1}^{N,S} \quad (36)$$

and visualise the memorisation ratio for various distance thresholds c in Figure 5 along with the distributions of generated samples, $p(\hat{x})$, $p_E(\hat{x})$ and $p_R(\hat{x})$. We report the KL-divergence to the target distribution p_* as a measure of generalisation.

C.1.1. COMPARING BIAS AND VARIANCE OF THE GENERATED DISTRIBUTIONS

In Figure 8 we fix $N = 1$ sample of x_0 and plot the mean and variance for the distribution of generated data samples obtained from the $S = 1000$ generators, as argued in Subsection 4.1. We observe that the Euclidean distribution has a bias and higher variance than the Riemannian distribution, as also seen in Figure 4. Both findings indicate that the Riemannian paths stay closer to the MAP solution, as theoretically argued in Subsection 4.3.

C.2. Toy Experiment in 2D

We consider the base distribution to be an isotropic Gaussian in \mathbb{R}^2 , i.e. $p_0 \sim \mathcal{N}(\mathbf{0}, \mathbb{I}_2)$, and the target distribution p_* to be a GMM with equally weighted means at $\mu_1 = [1.5, 1.5]^\top$ and $\mu_2 = [-1.5, -1.5]^\top$, both with covariance $\Sigma = 0.2 \cdot \mathbb{I}_2$. We train a network to memorise six points \mathbf{P}_i in total, three at each mode, such that for all i, j ,

$$\min_{k=1,2} \{\|\mathbf{P}_i - \mu_k\|\} = \min_{k=1,2} \{\|\mathbf{P}_j - \mu_k\|\}.$$

That is, the points \mathbf{P}_i all have the same distance to whichever μ_k they are closer to. A visualisation is shown in Figure 9.

We sample the base distribution as in the 1D toy example in Section 5 and choose the initial velocities to be along the eigenvector of the Hessian $\mathbf{H}_{\mathcal{L}}(\theta)$ corresponding to the highest eigenvalue, which intuitively corresponds to the most

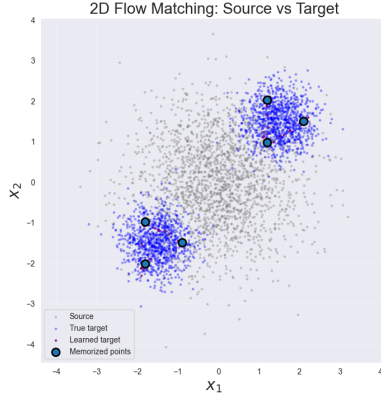


Figure 9. The source distribution p_0 samples are shown in grey, and the target distribution p_* (blue) samples in blue. The model learns to memorise the equidistant points \mathbf{P}_i (purple) from each mixture mode. In purple (purple), we show samples from the learnt distribution.

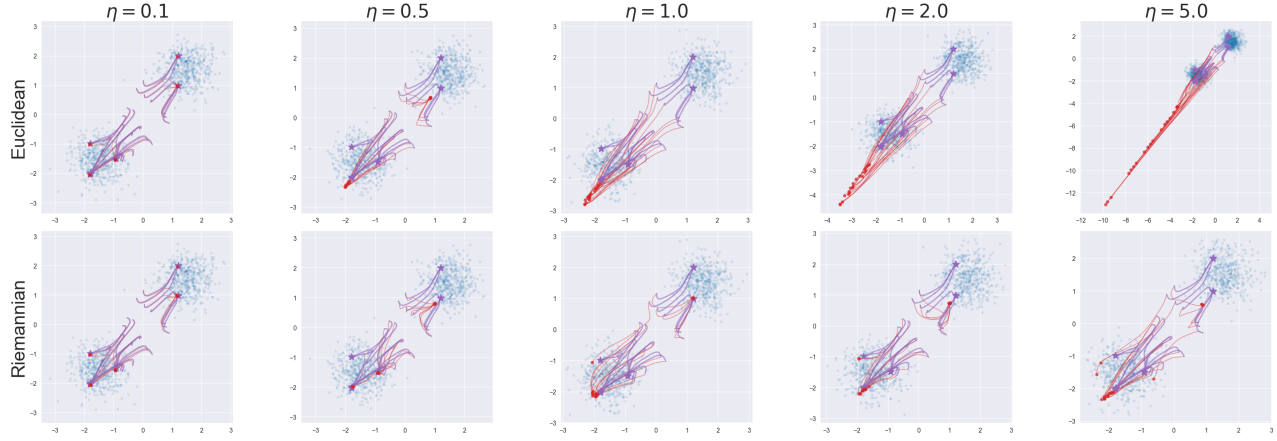


Figure 10. The blue points denote samples from the true target distribution p_* , and the purple lines are trajectories from the base distribution p_0 . The endpoints of the learnt model (MAP estimate) are represented by (red dot). The red lines correspond to the trajectories from the perturbed models (top row corresponding to linear and bottom to the geodesic perturbations), ending at $\hat{\mathbf{x}} = g_{\theta^s}(\mathbf{x}_0), \mathbf{x}_0 \sim p_0$ (red dot). As the magnitude of the initial velocity \mathbf{v} increases, the geodesic trajectories remain within favourable regions of the target space, whereas the Euclidean samples render trajectories that fall into low-density regions of p_* .

impactful direction to travel along the loss manifold. We explore different scaling levels η of the initial velocity vectors. The trajectories from p_0 to p_* given by the Euclidean Laplace and the Riemannian perturbation are shown in Figure 10.

Furthermore, we then sample 3000 points from p_0 and examine the endpoints following the Euclidean and Riemannian Laplace approximations, and MAP models by quantifying the empirical Wasserstein distribution between samples from the true target p_* and the generated samples $g_{\theta^s}(\mathbf{x}_0), \mathbf{x}_0 \sim p_0$. Recall the definition of the Wasserstein distance between two probability measures.

Definition C.1. (Villani et al., 2008) Let μ and ν be probability measures on a Polish metric space (\mathcal{X}, d) . Then the Wasserstein 1-distance between μ and ν is given by

$$W_1(\mu, \nu) = \inf_{\pi \in \Pi(\mu, \nu)} \int_{\mathcal{X}} d(x, y) d\pi(x, y) = \inf \{ \mathbb{E} d(X, Y), X \sim \mu, Y \sim \nu \}. \quad (37)$$

Following Peyré et al. (2019), this can be adapted to empirical measures $\mu = \frac{1}{n} \sum_{i=1}^n \delta_{\mathbf{x}_i}$ and $\nu = \frac{1}{m} \sum_{j=1}^m \delta_{\mathbf{y}_j}$ to obtain the Wasserstein 1-distance

$$W_1(\mu, \nu) = \inf_{\gamma \in \Pi(\mu, \nu)} \left\{ \sum_{i=1}^n \sum_{j=1}^m \gamma_{ij} \|\mathbf{x}_i - \mathbf{y}_j\|, \quad \sum_{j=1}^m \gamma_{ij} = \frac{1}{n}, \quad \sum_{i=1}^n \gamma_{ij} = \frac{1}{m}, \quad \gamma_{ij} \geq 0 \right\} \quad (38)$$

by choosing $d(x, y) = \|\mathbf{x} - \mathbf{y}\|_2$ to be the standard Euclidean distance on \mathbb{R}^2 .

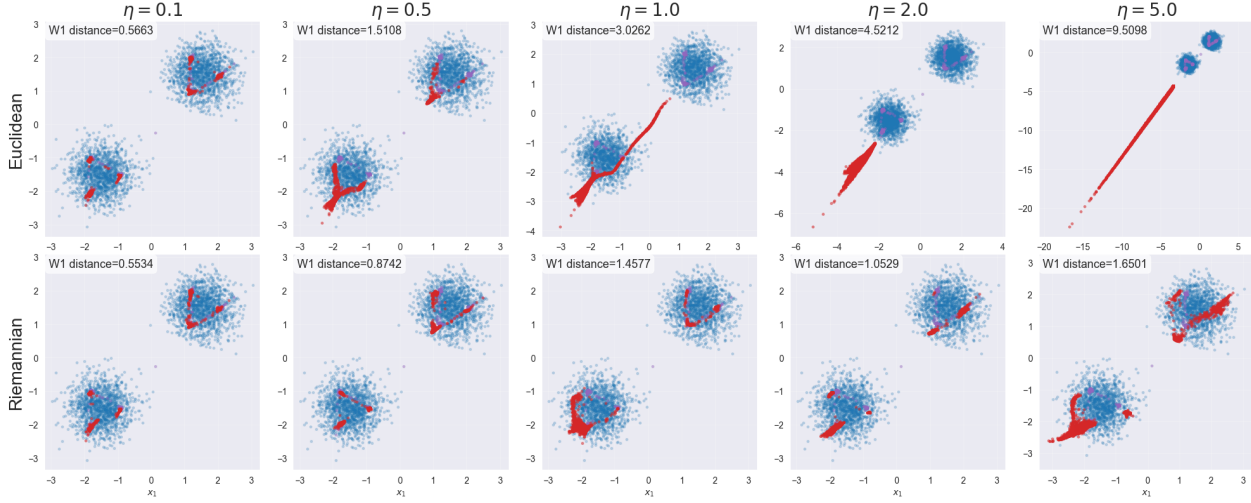


Figure 11. We compare 3000 points $\hat{x} = g_{\theta^s}(x_0)$, $x_0 \sim p_0$ (red dot) generated by the models sampled with the Euclidean Laplace approximation (top row) and the Riemannian Laplace approximation (bottom row) and show them in superposition with the samples generated by the MAP model g_{θ^*} (blue dot). The distribution of the points generated by the MAP model and the target distribution are at a Wasserstein 1-distance of 0.4348. We see that by increasing initial velocity scaling, points from the Euclidean setting fall in regions of low mass of p_* , and their distribution increases in Wasserstein distance to the p_* . Using the Riemannian Laplace approximation, the effect is remarkably milder.

D. Laplace Approximations for Generative Image Models

In this section, we show how we analysed memorisation exhibited by generative image models. We summarise our approach in Algorithm 2, and provide details in the following subsections.

D.1. Model Details

We use a time-conditioned 2D U-Net architecture with residual connections and a self-attention bottleneck, as commonly used in diffusion models (Ho et al., 2020)¹. The network follows an encoder-decoder U-Net design with four downsampling and four upsampling stages based on 3×3 convolutions with padding and striding of shape (1×1) . The stages are connected by skip connections. The network processes RGB inputs, conditions all residual blocks on a learned 512-dimensional time step embedding, and uses GroupNorm with SiLU activations throughout.

We found that a pre-trained model trained on the full dataset showed no memorisation. Therefore we choose a subset of 1000 randomly sampled images from CIFAR-10, normalised to the range $[-1, 1]$ and train the model for up to 5000 epochs using a learning rate of $2 \cdot 10^{-4}$ using the denoising diffusion probabilistic model (DDPM) scheduler with 1000 steps. We store checkpoints every 50th epoch and later generate images with 50 DDIM steps, using the model that we deem to balance memorisation and generalisation best, defined by the Frechét Inception Distance (FID) (Heusel et al., 2017).

D.2. Hessian Approximation in High Dimensions

Recall that the Laplace approximation is defined as a Gaussian $\mathcal{N}(\theta^*, \mathbf{H}^{-1})$ where θ^* is the MAP and $\mathbf{H}^{-1} := \mathbf{H}_{\mathcal{L}}^{-1}(\theta^*)$ is the inverse Hessian at the MAP. It should be noted that the inverse Hessian must be positive definite to be a valid covariance matrix. If so, we can sample from the approximate posterior using a reparameterisation trick:

$$\theta^s = \theta^* + \Sigma^{1/2} \epsilon, \quad \epsilon \sim \mathcal{N}(\mathbf{0}, \mathbb{I}_K).$$

In the context of deep neural networks, we face two problems related to drawing samples like this. First, the Hessian is in practice too large to keep and manipulate in memory. Second, the Hessian of a deep neural network is generally indefinite.

We solve the first problem by using a low-rank approximation of the Hessian, namely $\mathbf{H} \approx \mathbf{Q} \mathbf{T} \mathbf{Q}^\top$ where $\mathbf{Q} \in \mathbb{R}^{K \times k}$ and $\mathbf{T} \in \mathbb{R}^{k \times k}$ is a tridiagonal matrix. We determine these matrices with the matrix-free Lanczos iteration (Lanczos, 1950) with

¹Implementation taken from <https://huggingface.co/google/ddpm-cifar10-32>

Algorithm 2 Riemannian Bayesian Inference for Generative Models in High Dimensions

```

1: Input: Generator  $g_{\theta}$  with  $K$  parameters, twice-differentiable loss  $\mathcal{L}(\theta)$ , training data  $\mathcal{D}_x$ , batch size  $N$ , number of perturbations  $S$ , perturbation strength  $t$ , repetitions  $B$ , number of Lanczos iterations  $k \ll K$ .
2: Output: Generated images  $\{\hat{x}_{n,s,b}\}_{n=1,s=1,b=1}^{N,S,B}$ 
3: Step 1: MAP training
4:  $\theta^* \leftarrow \arg \min_{\theta} \mathcal{L}(\theta)$  {Train  $g_{\theta}$  using SGD}
5: for  $b = 1$  to  $B$  do
6:   Fix a batch of  $N$  training data  $\mathbf{X}_*^{(b)} = \{\mathbf{x}_*^n\}_{n=1}^N \sim \mathcal{D}_x$ , noise samples  $\mathbf{X}_0^{(b)} = \{\mathbf{x}_0^n\}_{n=1}^N$ , and time samples  $\mathbf{t}^{(b)}$ 
7:   Define batch loss:  $\mathcal{L}^{(b)}(\theta) := \mathcal{L}(\theta \mid \mathbf{X}_*^{(b)}, \mathbf{X}_0^{(b)}, \mathbf{t}^{(b)})$ 
8:   Step 2: Hessian approximation {Compute exact Hessian if feasible}
9:   Approximate Hessian  $\mathbf{H}_{\mathcal{L}} := \nabla_{\theta}^2 \mathcal{L}^{(b)}(\theta^*) \approx \mathbf{Q} \mathbf{T} \mathbf{Q}^{\top}$  using  $k$  Lanczos iterations.
10:  Eigendecompose  $\mathbf{T} = \mathbf{V} \Lambda \mathbf{V}^{\top}$  and restrict to positive pairs  $\Lambda_+$  and  $\mathbf{V}_+$ 
11:  Define  $q(\theta) = \mathcal{N}(\theta, \mathbf{H}_{\mathcal{L}}^{-1})$  using approximation  $\mathbf{H}_{\mathcal{L}}^{-1} \approx \mathbf{Q} \mathbf{V}_+ \Lambda_+^{-1} \mathbf{V}_+^{\top} \mathbf{Q}^{\top}$  {Laplace approximation}
12:  Step 3: Parameter perturbation
13:  for  $s = 1$  to  $S$  do
14:    Compute perturbation from the Laplace approximation:  $\mathbf{v} \leftarrow \mathbf{Q} \mathbf{V}_+ \Lambda_+^{-1/2} \mathbf{V}_+^{\top} \mathbf{Q}^{\top} \epsilon$  {Sample  $\epsilon \sim \mathcal{N}(\mathbf{0}_k, \mathbb{I}_k)$ }
15:    Compute parameter perturbation:
16:      Euclidean:  $\theta_{s,b} \leftarrow \theta^* + t \mathbf{v}$ 
17:      Riemannian:  $(\theta_{s,b}, \mathcal{L}(\theta_{s,b})) \leftarrow \text{Exp}_{h(\theta^*)}(t \cdot \mathbf{J}_h(\theta^*) \mathbf{v})$ 
18:  Step 4: Data generation
19:  Generate  $\hat{x}_{n,s,b} \leftarrow g_{\theta_{s,b}}(\mathbf{x}_0^n)$  from noise samples  $\mathbf{x}_0^n \in \mathbf{X}_0^{(b)}$ .
20: end for
21: end for

```

full re-orthogonalisation using $k = 1000$ Lanczos iterations. This approach only requires Hessian-vector products which are efficiently computed using automatic differentiation, and does not require storing the full Hessian in memory. Although the procedure in theory works for approximating the full Hessian of large networks, we note that the full re-orthogonalisation procedure requires keeping k vectors of K dimensions in the matrix \mathbf{Q} in memory, which is not feasible for the full network.

To address the second issue, note that we need the matrix square root of the inverse Hessian for sampling the Laplace posterior. We compute this through an eigendecomposition of the tridiagonal matrix, hence $\mathbf{T} = \mathbf{V} \Lambda \mathbf{V}^{\top}$ where \mathbf{V} contains the eigenvalues of \mathbf{T} which approximate the extremal eigenvalues of \mathbf{H} . Note, that this allows us to approximate the Hessian and its inverse by

$$\mathbf{H} \approx \mathbf{Q} \mathbf{V} \Lambda \mathbf{V}^{\top} \mathbf{Q}^{\top}, \quad \mathbf{H}^{-1} \approx \mathbf{Q} \mathbf{V} \Lambda^{-1} \mathbf{V}^{\top} \mathbf{Q}^{\top}.$$

As mentioned, the Hessian can easily be indefinite and so can its approximation. We deal with this in the naive way by removing all non-positive eigenvalues and their associated eigenvectors. We denote these by \mathbf{V}_+ and Λ_+ , and remark that the resulting Hessian approximation is positive definite. It is well known that every positive definite matrix is invertible, and its inverse is also positive definite. This further implies the existence of the square root of the inverse, in our case we obtain:

$$\mathbf{H}_+^{-1/2} \approx \mathbf{Q} \mathbf{V}_+ \Lambda_+^{-1/2} \mathbf{V}_+^{\top} \mathbf{Q}^{\top}.$$

This allows us to sample the velocity

$$\mathbf{v} = \mathbf{Q} \mathbf{V}_+ \Lambda_+^{-1/2} \mathbf{V}_+^{\top} \mathbf{Q}^{\top} \epsilon, \quad \epsilon \sim \mathcal{N}(0, \mathbb{I}_K),$$

which is used for computing both the Euclidean and Riemannian perturbation.

D.3. Generating Images with Perturbed Parameters on Stochastic Loss Manifolds

We are working with a high-dimensional model and a large dataset, hence we must resort to mini-batching, which means that we use a *stochastic* version of our method. We do so by defining a posterior loss manifold (as described in Subsection

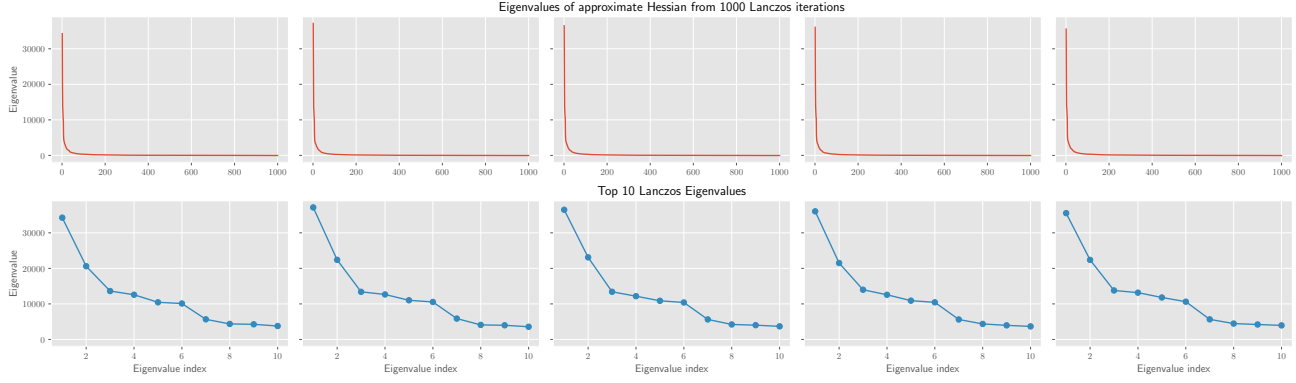


Figure 12. Eigenspectra of approximated Hessians, computed for 5 different batches of training data.

2.2.1) per batch of the training data, $\mathcal{D}_i \sim \mathcal{D}$. We additionally fix the initial samples $x_0 \sim p_0$ and the time step samples to ensure that stochasticity only comes from the batching operation.

We construct a manifold for B batches and follow the strategy of approximating the Hessian described above, resulting in B Riemannian Laplace approximations from which we can draw parameter perturbations. We plot the approximate eigenspectra for 5 such batches in Figure 12, using a batch size of 64. Although the spectra differ slightly, they all reflect that the Hessians are dominated by few highly curved directions and many near-zero directions.

To summarise, we perturb the model parameters by

1. defining the manifold for a data batch,
2. approximating the Hessian of this manifold,
3. solving the Riemannian perturbation with S initial velocity samples as explained in the previous subsections,
4. generating N images for each sample θ^s .

By repeating for B batches, we get $B \times S \times N$ generated images from which we can do analyses of images generated over all B batches or include uncertainty by studying batch-wise variations.

D.3.1. SENSITIVITY ISSUES IN THE GEODESIC COMPUTATION

We observe that solving the geodesic equation is sensitive to the numerical integrator used, as well as the magnitude of the sampled initial velocity vector. First, note that we only get valid results when using an adaptive step-size method, e.g. 5th-order Runge-Kutta method (Dormand and Prince, 1980), while fixed step size methods like the Euler scheme or the 4th-order Runge-Kutta with a 3/8 rule result in generating psychedelic noise images using the perturbed parameters. We hypothesise that this is due to the adaptive method being able to slow down when approaching the more curved directions. Secondly, for initial vectors of large magnitude, the numerical solution of the geodesic equation can be slow to converge, as the convergence threshold needs to be sufficiently low for the numerical integrator to find a good solution. In the interest of time, we choose to filter out samples displaying this behaviour, by setting a stopping time criteria when solving the geodesic equation.

D.4. Memorisation Results

We consider a single batch of 64 training samples and compute $S = 10$ perturbations according to the previous descriptions. For each perturbation we generate $N = 100$ images, resulting in a total of 1000 generated images from the ensemble. We compute the memorisation ratio with respect to the $|\mathcal{D}_i| = 1000$ randomly chosen training points, subject to a memorisation constant of $c = 1/3$. We extend the memorisation measure to consider the $K = 10$ next-closest images from the training set, rather than only the second-closest, since there are image duplicates in the training data. Similarly to the 2D case, we introduce a scaling parameter η when sampling the approximate posterior, however, we now do not limit samples to be along the top-eigenvector.

As seen in Figure 13, roughly 90% of the images generated using the MAP model are memorised. We also see the effect of perturbing the model parameters, in the sense that it reduces memorisation, no matter the perturbation strategy. Remarkably, the Riemannian perturbations reduce memorisation more than the Euclidean ones when increasing the magnitude of the initial velocity samples η . This surprised us, and we believe that it relates to the sensitivity of the numerical integrator, as described in the previous subsection.

When looking at a random selection of generated images using the MAP model, we clearly see why the memorisation ratio is that high (Figure 14). Using the same initial samples $x_0 \sim p_0$, we additionally see that perturbing the parameters using e.g. $\eta = 0.5$ results in noisier images, which is exactly a valid way to reduce memorisation according to its definition. Conceptually, one might however argue that the image concepts are still memorised. We hypothesise that this is related to the high memorisation rate of the MAP model, suggesting that it converged to a local minima which might be hard to escape from using the geodesics.

A MAP solution that memorises effectively learns to recreate the training data. Consequently, all models based on variations of the MAP are also able to recreate the training data, but the difference is that such models additionally introduce new characteristics that were not present in the training data. In the image domain, these characteristics should ideally be structured so as to meaningfully alter the underlying concept of the training image, for example by changing the time of day, the background, or the shape of the pictured object. However, while our approach can generate new images in the vicinity of the training data, it is not currently optimised for images and therefore does not constrain the new samples to lie on the image manifold. We hope to address this issue soon to further improve our method on the image domain.

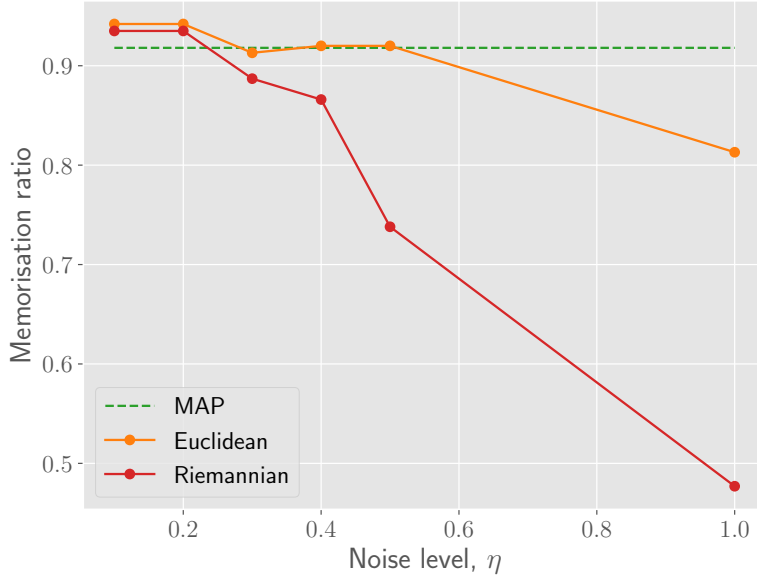


Figure 13. Memorisation reduces by perturbing the model parameters for a generative image model. This happens for both types of Laplace approximations defined from a single batch of training samples.

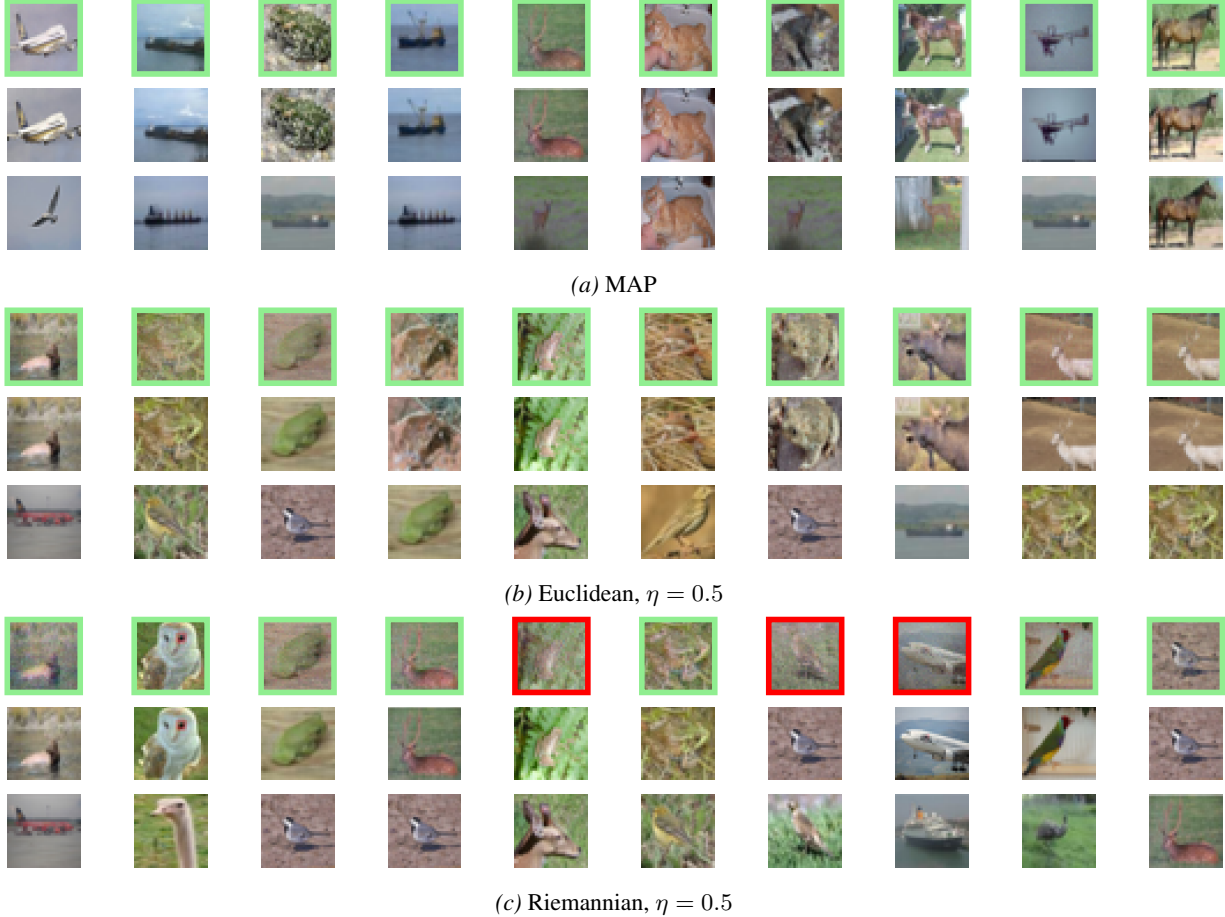


Figure 14. We show a random selection of generated images where each column uses the same initial sample $\mathbf{x}_0 \sim p_0$. For each of the three figures the top row corresponds to the generated images. The second and third row corresponds to the closest and second-closest images from the subsampled training set, respectively. Using a memorisation criteria of $c = 1/3$ and based on the $K = 10$ next-closest neighbours, we indicate whether a generated sample is memorised by framing it with a green box. If it is not memorised, we frame it by a red box. The Riemannian samples are memorised less often than the other approaches, which seems to only be due to added noise on the pixels. We hypothesise that the result depends on properties of the loss at the MAP and hence the MAP memorisation ratio.